für Angewandte Analysis und Stochastik

im Forschungsverbund Berlin e.V.

Preprint ISSN 0946 – 8633

Experimental and Numerical Investigation of Edge Tones

Andreas Bamberger[1], Eberhard Bänsch[2], Kunibert G. Siebert[3]

submitted: September 30, 2001

[1] Fakultät für Physik
Universität Freiburg
Hermann-Herder-Str. 3
D-79104 Freiburg
E-Mail: bamberger@physik.uni-freiburg.de

[2] Weierstraß-Institut für
Angewandte Analysis und Stochastik
Mohrenstr. 39
D-10117 Berlin
E-Mail: baensch@wias-berlin.de

[3] Institut für Angewandte Mathematik
Universität Freiburg
Hermann-Herder-Str. 10
D-79104 Freiburg
E-Mail: Kunibert.Siebert@mathematik.uni-freiburg.de

Preprint No. 681
Berlin 2001

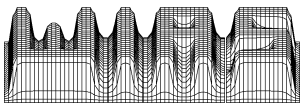

1991 *Mathematics Subject Classification.* 65N30.

Key words and phrases. Edge tones, experimental investigation, numerical methods, Navier-Stokes equations, adaptive finite elements.

Edited by
Weierstraß–Institut für Angewandte Analysis und Stochastik (WIAS)
Mohrenstraße 39
D — 10117 Berlin
Germany

Fax: + 49 30 2044975
E-Mail (X.400): c=de;a=d400-gw;p=WIAS-BERLIN;s=preprint
E-Mail (Internet): preprint@wias-berlin.de
World Wide Web: http://www.wias-berlin.de/

Abstract. We study both, by experimental and numerical means the fluid dynamical phenomenon of so-called edge tones. Of particular interest is the clarification of certain scaling laws relating the frequency f to geometrical quantities, namely d, the height of the jet, w, the stand–off distance and the velocity of the jet. We conclude that the Strouhal number S_d is given by $S_d = C \cdot (d/w)^n$ with $n \approx 1$ in our case. Moreover, the constant C of the experiment agrees within 10–15% with the result of the simulation. As for the frequency dependence on the geometry and on the jet velocity there is a very good agreement of experimental and numerical results.

1. Introduction

Edge tone is a fluid dynamical phenomenon which develops as a jet leaves a flue and encounters an edge. This may result in an oscillatory behaviour of the jet due to positive fluid dynamical feedback. Similarly, when a flow traverses a shallow wall cavity a so called cavitone may be produced. In this paper we investigate the edge tone phenomenon by experiment as well as by numerical simulation.

The phenomenon addressed here is a fluid dynamical problem which is based on an instability of the flow due to shear layers. The situation can be characterized by the Reynolds number which is large compared to one, so that the transverse perturbation is able to cross a certain characteristic distance of the configuration without being damped away. As the Reynolds number further increases and surpasses a critical value the system enters into another regime, turbulence becomes dominant [19]. In this investigation we are well within the regime of instability, but below turbulence. The flow seems to be laminar at small perturbations, but due to the growing instability there is a breakdown of the laminar flow and flow separation occurs (pseudo-laminar flow).

At certain conditions periodic movement due to the positive feedback mechanism occurs and creates audible acoustical waves. For this reason the edge tone phenomenon was observed for some time, see for instance Sondhaus [31] and Brown [7]. Scaling laws relating the frequency with the geometry and the jet speed have been suggested already in [7].

Particularly obvious are the main features by the simplifying consideration first stated by Powell [26]: A perturbation of the jet with speed U finally results in a vortex further downstream. It travels with a phase velocity c_p and encounters the edge at the stand–off distance w. Here the vortex interacts and radiates an acoustical wave feeding back upstream to the region of the nozzle. The same picture holds as a flow passes across a shallow cavity since the leading and trailing edge is coupled in the same way. The oscillatory behaviour with the frequency f is related with the phase velocity of both, the acoustical wave c_0 as well as the perturbation. The *Rossiter equation* [28] reads

$$w/c_p + w/c_0 = k/f, \qquad k = 1, 2, 3, \ldots, \tag{1}$$

where the index k is constant for a "stage" or fluid dynamical mode. From experiments it appears that k has to be replaced by $(k - \beta)$, β being a phase offset. As a result the above relation would yield

$$S_w = (k - \beta)/(U/c_p + M) \tag{2}$$

in terms of the Strouhal number $S_w = wf/U$, where $M = U/c_0$ is the Mach number. In our case c_0 is much larger than c_p. Typical values for c_p/U are between $0.4 - 0.6$. Our prime interest in this investigation is focussed on the "Stage I", or the fundamental fluid dynamical mode $k = 1$.

Scaling laws of the above type have been derived from experimental data by Brown [7], Nyborg and others [1, 24]. As mentioned above a justification of such a law has been formulated in [26] and later followed up in [18]. Moreover Holger [14] and Crighton [10] state a more general law in terms of the Strouhal number S_d given here for $k = 1$:

$$S_d = \frac{f \cdot d}{U_0} = C \cdot (d/w)^n, \tag{3}$$

where d is the height of the nozzle, U_0 the maximum velocity at the exit of the nozzle. The constant C behaves like $C \sim (1-\beta)(c_p/U)$ for small Mach numbers.

The exponent n in (3) is the prime subject of this investigation. In former experiments it was shown to be between 1 and 3/2, depending on the experimental configuration. There are two explanations for a behaviour with $n > 1$ depending on the state of turbulence of the jet.

(1) At low Reynolds numbers the flow is pseudo-laminar. As will be argued below, the phase velocity can be derived from linear instability theory through dispersion relations. From this its frequency dependence results in $n \approx 1$.
(2) As observed by Carriere [8] and Jones [16] there is a slowing down of the jet velocity itself and therefore a decrease of the wave length of the disturbance would produce a power larger than one. This may happen if the jet is highly turbulent and loses momentum. As can be shown, this results in $n \leq 3/2$ and would be encountered at higher Reynolds numbers.

Our investigation deals with moderate Reynolds numbers, namely $113 \leq Re_d \leq 873$ in the experiment and $171 \leq Re_d \leq 912$ in the simulation, and Strouhal numbers $0.028 \leq S_d \leq 0.177$ and $0.027 \leq S_d \leq 0.077$ respectively. Hence, rather the situation $n \simeq 1$ is expected.

The problem addressed here was treated theoretically by linear instability theory on the basis of the Raleigh equation [11]. Generally, a free jet develops an instability after leaving the nozzle. There are two eigenmodes: a symmetric, sinusoidal and an asymmetric, varicose mode with exponentially increasing amplitudes. They are obtained analytically with a spatial solution by Mattingly and Criminale [21]. The first mode is the dominating one. It deflects the jet in the transverse direction with respect to the primary direction. If the jet encounters a sheet or a wedge like edge the deflection produces a backward reaching velocity field which feeds back to the jet at the nozzle. A stable oscillatory condition occurs as the resulting distortion reaches the edge at a proper transit time producing a phase lock feedback cycle. In order to produce a stable condition the stand–off distance w has to be of the order of a wave length $\lambda = c_p \cdot f$. This spatial description was experimentally proven by [23] to be the preferred one in contrast to the temporal description given for instance by [29].

For the understanding of the power dependence in (3) and the phase offset β the derivations of Holger [14] and Crighton [10] are relevant. The former include experimentally determined parameters in order to achieve a value for the constant C. There is some overall agreement with data given in [7, 24]. Crightons derivation is without any adjustable parameters and overestimates the constant C by an order of magnitude. Both, however, work with a low frequency approximation of the dispersion relation: at very low frequencies the phase velocity c_p behaves like $c_p \sim S_d^{1/3}$, which leads to an exponent $n = 3/2$. In fact, the low frequency approximation taken from the temporal solution is actually mentioned as a possible cause for the overestimation of the constant C in [10]. In contrast to these results a closer look at the experiments shown for comparison rather displays a $n = 1$ behaviour [1, 7, 24]. This behaviour is already explicitly stated in [7] in a similar expression like (3) with $n = 1$.

A recent theoretical calculation by Howe [15] using a linearized analysis, in which free shear layers, representing a thin jet, are treated as vortex sheets, again states $n = 3/2$ for the w dependence. However, it is mentioned that the thin jet approximation is not applicable for small stand-off distances which is usually relevant for the fundamental fluid dynamical mode.

Generally, there is an uncertainty with respect to the dependence of the height d of the flue and the velocity profile of the jet as it leaves the exit of the nozzle. Theoretical calculations often assume ideal conditions as flat hat shape, or Bickley profile. In [10] and [15] the Kutta condition at the nozzle exit is used for the calculation resulting in a straight continuation of the jet at this point.

At this point new experiments and computational simulations were in order for a clarification of the behaviour of the exponent n. The mathematical model used for the simulations are the

incompressible Navier-Stokes equations. Within linear instability analysis the growth of three-dimensional perturbations are less amplified than two-dimensional perturbations [11]. Thus, we are using the two dimensional Navier-Stokes equations for sake of saving computing time. The incompressibility condition is well justified considering low Mach numbers $M < 0.05$. Since we are dealing with moderate Reynolds numbers, viscous effects cannot be neglected and are treated by the numerical method. The detailed comparison of the simulation with the experiment is important with respect to the assumptions made in our model.

As can be seen from (1) a positive feedback loop may be formed by more than one value k for a given ratio of k/f. There is one dominant frequency and therefore the frequency jumps at certain distances. Furthermore, a hysteresis effect is associated with these jumps which has been observed experimentally in this investigation.

The aim of this paper can be summarized as follows:

- A verification of the scaling law and its constant C by experiment and simulation. The reproduction of the constant C is one of the major achievements of this investigation.
- A clarification of the $1/w$-behaviour. The exponent $n \simeq 1$ has been observed in this investigation, both by the experiment and the simulation.

In our investigation we concentrate on the first fluid dynamical mode for reasons of simplicity. The detailed understanding of edge tone phenomena in general might also be useful in applications as fluid velocimetry from edge tone frequency.

Finally, the importance of the edge tone phenomena may be stated in relation with flute like wind instruments. The oscillatory pressure difference at the edge creates the acoustical wave. In presence of a resonator the acoustical field is amplified and takes over the feed back loop. In wind instruments, like organ pipes the edge tone often plays an important role in the transitory regime of the onset of response [9].

The paper is organized as follows: In § 2 we describe the experimental setup and the experimental measurement procedure. The discretization and the used solver for the numerical simulation as well as the numerical measurement procedure are explained in § 3. In § 4 we present and compare the results of the experiment and the simulation both proving a $n = 1$ behaviour in (3). We conclude the paper with a short summary in § 5.

2. Experimental setup

The investigations are carried out in a relatively low velocity regime. The effort is concentrated on the first fluid dynamical mode, which is an experimental challenge for moderate aspect ratios like w/d=3.5. For the experimental arrangement see Figure 1.

The setup consists of a flue with two possible cross sections of 1×10 mm^2 and 0.5×10 mm^2, respectively. The length of the flue is 150 mm. It is chosen long enough in order to guarantee the parabolic velocity profile of the jet at the outlet.

The edge consists of a wedge with an angle of $\alpha = 23^0$ as shown in Figure 1. The position for the stand-off distance w is adjustable by micro meter screws with a precision of 0.05 mm. The offset ε from the lower edge of the flue is also adjustable with the same precision.

The arrangement is such that any extended object is at a distance of more than 20 cm. This way unwanted acoustical feedback is suppressed. A number of preparative experiments proved the following conditions:

- The lateral extension of the jet with 10 mm is proven to be large enough by changing this quantity down to 5 mm without sizeable change of the frequency.
- The use of smaller length of the flue gave the same results.

- The Schlieren method together with a stroboscopic illumination is used to visualize the jet. Indeed the jet appeared to be not turbulent.

Air is used as medium and supplied from a bottle. The pressure is regulated by a precision valve. The pressure of the air at the entrance of the flue is measured for reference with a water manometer.

The velocity of the jet is determined by a hot wire anemometer (DANTEC C35) at a distance 1 mm downstream of the flue exit. During the measurement of edge tones the anemometer is retracted above exit of the flue in order to avoid any disturbance. The calibration is done with a Pitot tube in an independent setup for velocities ranging between 2 and 20 m/s. The accuracy of the calibration is estimated to be about ± 0.5 m/s.

In order to be independent of the acoustical power produced by the jet movement the oscillation is measured near the edge by a pressure sensor (KULITE 9322M). The size of the opening leading to the sensor near the edge is only 0.4 mm in diameter, see Figure 1.

The amplified signal, typically 20 mV/Pa is fed into a spectrum analyser (TEKTRONIX 2642A) in order to determine the frequency of the fundamental. The sensitivity gained by this setup is considerable as compared with a microphone positioned at some distance, specially at the onset of the periodic movement at low stand-off distance w. The frequency determination is done with the spectral analyzer with a precision of 1% in the frequency range covered in this experiment.

2.1. **Procedure of the Measurement.** The measurements are done in the following way: The velocity profile of the jet is checked in the condition, where the edge is removed, at a distance of 1 mm from the outlet. The profile is to a good approximation parabolic with negligible wings.

For the measurements at a given jet velocity of a given flue cross section the maximum velocity at the center of the flue is determined.

The frequency is measured as a function of the edge distance from the flue within the limits of the closest distance yielding a self sustained periodic signal and the change into the higher fluid

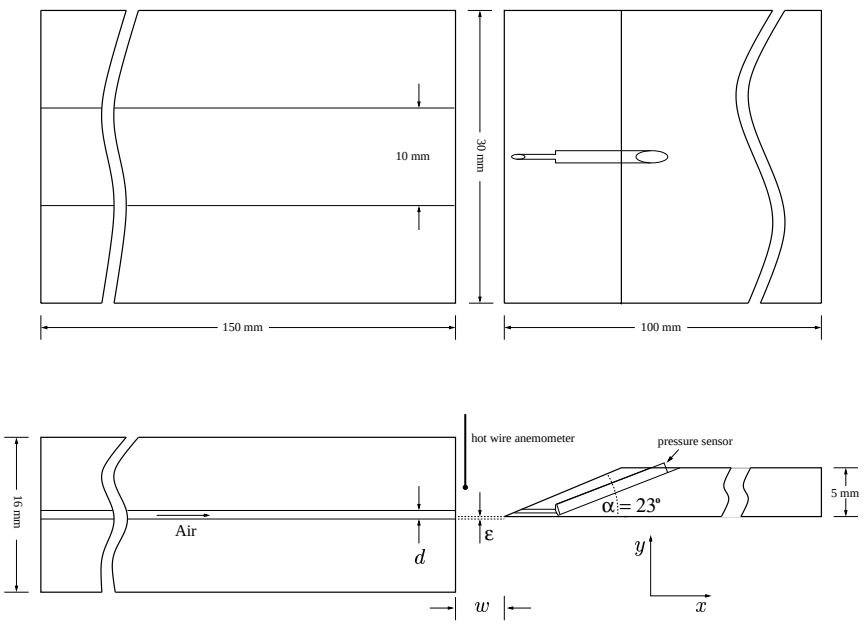

FIGURE 1. Experimental setup. Above: top view, below: side view. The edge tone signal is derived from the pressure sensor near the edge.

dynamic mode. This is observed by the appearance of an additional peak in the frequency spectrum not being a harmonic partial of the prominent frequency.

It is observed that the frequencies near the transition point deviate from the general $1/w$-law. This transition region is observed to be typically 0.5 mm and not taken into account for the comparison with the simulations.

The frequency measurements as a function of the distance w are done for different jet velocities ranging from 3.4 m/s to 13.0 m/s. The variation of w is between 2 mm to 9 mm.

Two sets of measurements corresponding to the different heights of the jet $d = 0.5$ mm and $d = 1.0$ mm are performed.

For a given height the offset ε is adjusted by the following procedure. Within the limits of $\varepsilon \simeq 0$ and $\varepsilon \simeq d/2$ the periodic movement of the jet is observed to be stable. For the frequency measurement it then is set about halfway between these limits, i.e. for $d = 0.5$ mm the offset is chosen as $\varepsilon = 0.13$ mm and $\varepsilon = 0.25$ mm for $d = 1.0$ mm. It is observed that the change of frequency is moderately small: less than 5% lower frequency at the limits of stable periodic operation of the jet. Small changes in ε yield nearly no changes in the measured frequencies.

3. Numerical simulation

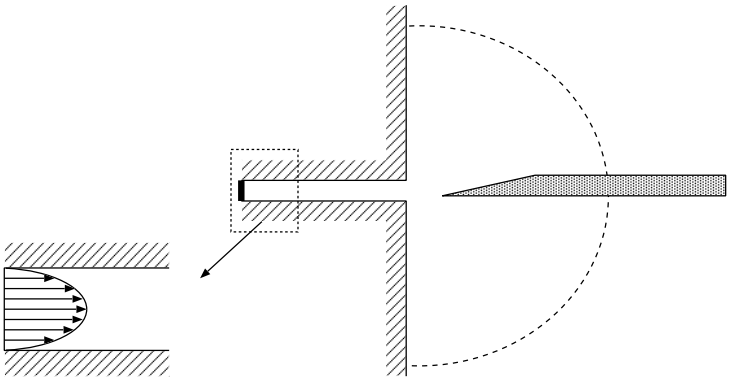

FIGURE 2. Geometry and parabolic inflow profile for the simulation. The inlet is indicated by the bold line and the restriction to the bounded computational domain by the dotted arc. The parabolic inflow profile is shown as a zoom.

As outlined in § 1 we use the two dimensional incompressible, isothermal Navier-Stokes equations as the mathematical model for the simulations: Find the velocity field $\boldsymbol{u}$ and pressure p such that

$$\partial_t \boldsymbol{u} - \nu \Delta \boldsymbol{u} + (\boldsymbol{u} \cdot \nabla)\, \boldsymbol{u} + \frac{1}{\rho} \nabla p = \boldsymbol{0} \quad \text{in } \Omega,\ t > 0, \tag{4a}$$

$$\operatorname{div} \boldsymbol{u} = 0 \quad \text{in } \Omega, \tag{4b}$$

where the (unbounded) domain Ω is shown in Figure 2. The parameters describing Ω, such as the stand–off distance w, the height of the nozzle d, etc., are as in Figure 1, $\nu = 1.535\mathrm{e}^{-5}[\mathrm{m}^2/\mathrm{s}]$ is the kinematic viscosity and $\rho = 1.188\ [\mathrm{kg}/\mathrm{m}^3]$ the density of air at 20° C and 1.0 $[10^5\mathrm{Pa}]$.

A parabolic inflow profile for the velocity is prescribed on the inflow boundary, indicated by the bold line in Figure 2:

$$\boldsymbol{u}(x, \cdot) := U_0 \frac{x_2 - y}{d} \left(1 - \frac{x_2 - y}{d}\right) \begin{pmatrix} 1 \\ 0 \end{pmatrix}. \tag{5}$$

Here, U_0 is the maximal inflow velocity and y the position of the bottom of the inflow channel. On the solid walls of the domain and on the surface of the labium we assume no-slip boundary conditions for the velocity.

In order to obtain a bounded computational domain for the numerical simulation, we intersect Ω with some ball of radius R, where R is chosen sufficiently large. This introduces an artificial boundary, indicated by the dotted line in Figure 2. On this artificial boundary we use a so called 'transparent' boundary condition [13].

Equation (4) is scaled to dimensionless variables by using the maximal inflow velocity U_0 [m/s] as a *characteristic velocity*, d [mm] as a *characteristic length* and $T = \frac{d}{U_0}$ as a *characteristic time scale*. Introducing the dimensionless variables

$$\hat{x} = \frac{x}{d}, \quad \hat{t} = \frac{t}{T}, \quad \hat{\boldsymbol{u}} = \frac{\boldsymbol{u}}{U_0}, \quad \text{and} \quad \hat{p} = \frac{p}{\rho U_0^2},$$

the dimensionless Navier-Stokes equations read

$$\partial_{\hat{t}} \hat{\boldsymbol{u}} - \frac{1}{Re_d} \hat{\Delta} \hat{\boldsymbol{u}} + (\hat{\boldsymbol{u}} \cdot \hat{\nabla}) \, \hat{\boldsymbol{u}} + \hat{\nabla} \hat{p} = \boldsymbol{0} \qquad \text{in } \hat{\Omega}, \ \hat{t} > 0, \tag{6a}$$

$$\hat{\operatorname{div}} \, \hat{\boldsymbol{u}} = 0 \qquad \text{in } \hat{\Omega}, \ \hat{t} > 0, \tag{6b}$$

where $Re_d = U_0 \, d/\eta$ is the Reynolds number and $\hat{\Omega}$ is the domain $\Omega \cap B_R$ scaled by $1/d$.

Denote by $\hat{\Gamma}_D$ the union of the solid walls of $\hat{\Omega}$, the surface of the labium, and the inflow boundary. Let $\hat{\Gamma}_N$ be the artificial boundary. Defining $\hat{\boldsymbol{g}}$ to be the scaled parabolic inflow profile (5) on the inflow boundary

$$\hat{\boldsymbol{g}}(\hat{x}) := (\hat{x}_2 - \hat{y}) \ (1 - (\hat{x}_2 - \hat{y})) \begin{pmatrix} 1 \\ 0 \end{pmatrix}$$

and $\boldsymbol{0}$ on the other parts of $\hat{\Gamma}_D$ we use the following boundary values:

$$\hat{\boldsymbol{u}} = \hat{\boldsymbol{g}} \qquad \text{on } \hat{\Gamma}_D, \ \hat{t} > 0, \tag{6c}$$

$$\frac{1}{Re_d} \partial_{\boldsymbol{n}} \hat{\boldsymbol{u}} + \hat{p} \, \boldsymbol{n} = \boldsymbol{0} \qquad \text{on } \hat{\Gamma}_N, \ \hat{t} > 0. \tag{6d}$$

In the sequel we omit the '^' and use the notation $\boldsymbol{u}$, p etc. for the scaled variables for simplicity.

3.1. **Adaptive finite element methods.** For the numerical solution of (6) we use an adaptive finite element method. For the discretization of parabolic problems we combine a discretization in space with finite elements on an underlying conforming triangulation consisting of triangles with an appropriate discretization in time.

Given some tolerance for the error between the discrete and true solution, the aim of an adaptive method is the efficient approximation of the solution within this prescribed tolerance. In each time step the underlying triangulation is adapted in such a way that it is fine in regions where a high resolution is needed but it still is as coarse as possible in all other regions.

Since the true solution is not known, information about the error between discrete and true solution has to be obtained by computable quantities. This goal can be achieved by *a posteriori* error indicators, which involve only information about the discrete solution and data of the problem and are thus *computable* [32]. A posteriori error indicators give information about the total error as well as local contributions on single mesh elements.

The adaptive method uses such indicators for the adaptation of the grids. The meshes are optimized by local refinement and coarsening of mesh elements (and reduction or enlargement of the time step size, if appropriate). The aim of this optimization is the equidistribution of local contributions over mesh elements while the error is below the given tolerance.

Starting with an initial grid $\mathcal{T}_0$, we construct a sequence of conforming triangulations $\mathcal{T}_{n+1}$ of Ω at time $t_{n+1} := (n+1)\tau$. For the time step (t_n, t_{n+1}), the discrete problem is solved in finite element spaces on $\mathcal{T}_{n+1}$.

In each time step, the adaptive algorithm iteratively solves the discrete problem, estimates the error, and adapts the mesh (and time step size) until the given tolerance is reached. We start with the mesh from the last time step. The mesh adaption is performed by local refinement and coarsening, using bisection (compare Figure 3) [3, 30]. All elements T with large local error

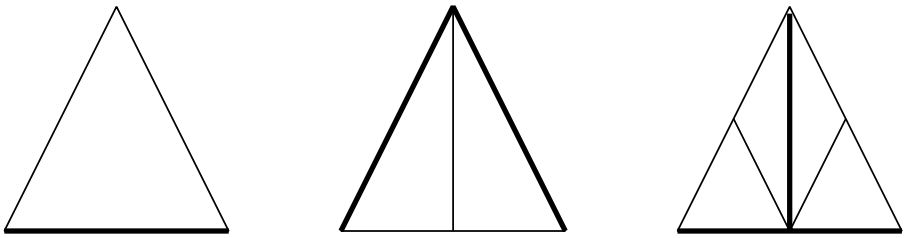

FIGURE 3. Iterative bisection of a triangle. Due to the passing on of the refinement edges (indicated by the bold lines) from parent to children, the minimum angle is uniformly bounded from below for all descendants.

indicator are marked for refinement and those elements T with local indicators much smaller than the local tolerance are marked for coarsening. If the grid is refined, the discrete problem is solved again, and the adaptive process is iterated. Usually, only a small number of adaptive iterations are needed in each time step. If the changes of the solution in time are very small, an *explicit adaptive strategy* is also sufficient, where the problem is solved only once in each time step. For our problem it turned out that it is even sufficient to perform a mesh adaptation every 3 time steps. For more details about adaptive methods we refer to [30].

3.2. **Discretization of the Navier-Stokes equations.**

3.2.1. *Time discretization.* Since we are studying highly transient flows the choice of the time discretization is crucial. First order methods are not appropriate due to their strong numerical dissipation. We use the so called fractional θ-scheme which was introduced in [6]. For an appropriate choice of θ and α (see below) this scheme is strongly A-stable and (nearly) non-dissipative, see e.g. [22]. Furthermore, we use this scheme in a variant as operator splitting, which decouples the two fundamental difficulties in the numerical treatment of the Navier-Stokes equations: the solenoidal condition and the nonlinearity. Each time step is split into three fractional steps. In the first and third step we compute a divergence free velocity field with corresponding pressure by solving a *linear saddle point problem* and handling the nonlinearity explicitly. In the second step we disregard the solenoidal condition and solve a *non-linear elliptic problem* for the velocity. The stability and convergence properties of this scheme for the time discretization of the Navier-Stokes equations are analyzed in [12, 17, 22].

The fractional θ-scheme reads: Let $\theta = 1 - \sqrt{2}/2$, $\theta' = 1 - 2\theta$, let $\alpha \in (\frac{1}{2}, 1)$ and $\beta = 1 - \alpha$.

For $n \geq 0$ and for $s = \theta, 1-\theta, 1$ define $\boldsymbol{g}^{n+s} := \boldsymbol{g}(\cdot, t_n + s\,\tau)$. Compute approximations $\boldsymbol{u}^n$ to $\boldsymbol{u}(\cdot, t_n)$ and p^n to $p(\cdot, t_n)$ in the following way. For $n = 0$ set

$$\boldsymbol{u}^0 = \boldsymbol{u}_0 \tag{7}$$

and for $n > 0$ calculate $(\boldsymbol{u}^{n+1}, p^{n+1})$ from $(\boldsymbol{u}^n, p^n)$ in three steps (compare Fig. 4):

Step 1: Define

$$\boldsymbol{f}^{n+\theta} := \frac{1}{\theta\,\tau}\boldsymbol{u}^n + \frac{\beta}{Re_d}\Delta\boldsymbol{u}^n - (\boldsymbol{u}^n \cdot \nabla)\boldsymbol{u}^n \tag{8a}$$

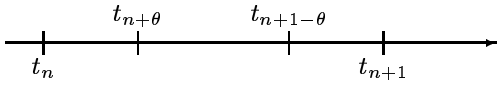

FIGURE 4. Subdivision of one time step for the θ-scheme.

and solve the *linear saddle point* problem

$$\frac{1}{\theta\,\tau}\boldsymbol{u}^{n+\theta} - \frac{\alpha}{Re_d}\Delta\boldsymbol{u}^{n+\theta} + \nabla p^{n+\theta} = \boldsymbol{f}^{n+\theta}, \qquad \operatorname{div}\boldsymbol{u}^{n+\theta} = 0 \tag{8b}$$

in Ω with boundary conditions

$$\frac{\alpha}{Re_d}\partial_{\boldsymbol{n}}\boldsymbol{u}^{n+\theta} + p^{n+\theta}\boldsymbol{n} = \boldsymbol{0} \quad \text{on } \Gamma_N, \qquad \boldsymbol{u}^{n+\theta} = \boldsymbol{g}^{n+\theta} \quad \text{on } \Gamma_D. \tag{8c}$$

Step 2: Define

$$\boldsymbol{f}^{n+1-\theta} := \frac{1}{\theta'\,\tau}\boldsymbol{u}^{n+\theta} + \frac{\alpha}{Re_d}\Delta\boldsymbol{u}^{n} - \nabla p^{n} \tag{9a}$$

and solve the *nonlinear elliptic* problem

$$\frac{1}{\theta'\,\tau}\boldsymbol{u}^{n+1-\theta} - \frac{\beta}{Re_d}\Delta\boldsymbol{u}^{n+1-\theta} + (\boldsymbol{u}^{n+1-\theta}\cdot\nabla)\boldsymbol{u}^{n+1-\theta} = \boldsymbol{f}^{n+1-\theta} \tag{9b}$$

in Ω with boundary conditions

$$\frac{\beta}{Re_d}\partial_{\boldsymbol{n}}\boldsymbol{u}^{n+1-\theta} = -p^{n+\theta}\boldsymbol{n} \quad \text{on } \Gamma_N, \qquad \boldsymbol{u}^{n+1-\theta} = \boldsymbol{g}^{n+1-\theta} \quad \text{on } \Gamma_D. \tag{9c}$$

Step 3: Define

$$\boldsymbol{f}^{n+1} := \frac{1}{\theta\,\tau}\boldsymbol{u}^{n+1-\theta} + \frac{\beta}{Re_d}\Delta\boldsymbol{u}^{n+1-\theta} - (\boldsymbol{u}^{n+1-\theta}\cdot\nabla)\boldsymbol{u}^{n+1-\theta} \tag{10a}$$

and solve the *linear saddle point* problem

$$\frac{1}{\theta\,\tau}\boldsymbol{u}^{n+1} - \frac{\alpha}{Re_d}\Delta\boldsymbol{u}^{n+1} + \nabla p^{n+1} = \boldsymbol{f}^{n+1}, \qquad \operatorname{div}\boldsymbol{u}^{n+1} = 0 \tag{10b}$$

in Ω with boundary conditions

$$\frac{\alpha}{Re_d}\partial_{\boldsymbol{n}}\boldsymbol{u}^{n+1} + p^{n+1}\boldsymbol{n} = \boldsymbol{0} \quad \text{on } \Gamma_N, \qquad \boldsymbol{u}^{n+1} = \boldsymbol{g}^{n+1} \quad \text{on } \Gamma_D. \tag{10c}$$

3.2.2. *The fully discrete equations.* The fully discretized system is a finite element approximation of the weak formulation for the fractional θ-scheme (8)–(10). Note that the transparent boundary conditions on Γ_N are *natural* boundary conditions in the weak equations (compare Sections 3.2.3 and 3.2.4).

We use the Taylor-Hood element on an adapted triangulation $\mathcal{T}_n$ of Ω for time step $(t_n,\, t_{n+1})$, i.e. the discrete velocity space $\boldsymbol{X}_n$ is given by

$$\boldsymbol{X}_n = \left\{\boldsymbol{\Phi} \in C^0(\bar{\Omega};\, \mathbb{R}^d);\ \boldsymbol{\Phi}_{|T} \in \mathbb{P}_k(T;\, \mathbb{R}^2),\ T \in \mathcal{T}_n,\ \boldsymbol{\Phi} = \boldsymbol{0} \text{ on } \Gamma_D\right\}$$

and the discrete pressure space Y_n by

$$Y_n = \left\{\Psi \in C^0(\bar{\Omega});\ \Psi_{|T} \in \mathbb{P}_1(T),\ T \in \mathcal{T}_n,\ \textstyle\int_\Omega \Psi\, dx = 0\right\},$$

where $\mathbb{P}_k$ denotes the space of polynomials of degree k, $k = 1, 2$. In the following we denote by $\{\boldsymbol{\Phi}_1, \ldots, \boldsymbol{\Phi}_{N_n}\}$ the usual nodal basis of $\boldsymbol{X}_n$, by $\{\Psi_1, \ldots, \Psi_{M_n}\}$ the basis of Y_n and by $\boldsymbol{X}_n^*$ and Y_n^* the dual spaces of $\boldsymbol{X}_n$ and Y_n respectively.

3.2.3. *The solution of the linear saddle point problem.* Define the linear operators $A_n\colon \boldsymbol{X}_n \to \boldsymbol{X}_n^*$ by

$$\langle A_n \boldsymbol{\Phi}_i,\, \boldsymbol{\Phi}_j \rangle = \frac{1}{\theta\tau} \int_\Omega \boldsymbol{\Phi}_i\, \boldsymbol{\Phi}_j\, dx + \frac{\alpha}{Re_d} \int_\Omega \nabla \boldsymbol{\Phi}_i\, \nabla \boldsymbol{\Phi}_j\, dx$$

for all $i, j = 1, \ldots, N_n$ and $B_n\colon Y_n \to \boldsymbol{X}_n^*$ by

$$\langle B_n \Psi_i,\, \boldsymbol{\Phi}_j \rangle = -\int_\Omega \Psi_i\, \operatorname{div} \boldsymbol{\Phi}_j\, dx$$

for all $i = 1, \ldots, M_n$, $j = 1, \ldots, N_n$.

Note that by the above *variational formulation* the outflow condition (6d) is incorporated as a natural boundary condition.

Denote by $B_n^*\colon \boldsymbol{X}_n \to Y_n^*$ the adjoint operator of B_n. For $s = \theta, 1$ (first and third step of the fractional θ-scheme, respectively), we have to solve the following *linear saddle point* problem: Find $\boldsymbol{U}^{n+s} \in \boldsymbol{g}^{n+s} + \boldsymbol{X}_n$ and $P^{n+s} \in Y_n$ such that

$$\begin{bmatrix} A_n & B_n \\ B_n^* & 0 \end{bmatrix} \begin{bmatrix} \boldsymbol{U}^{n+s} \\ P^{n+s} \end{bmatrix} = \begin{bmatrix} \boldsymbol{F}^{n+s} \\ 0 \end{bmatrix} \qquad \text{in } \boldsymbol{X}_n^* \times Y_n^*, \tag{11}$$

where the functional $\boldsymbol{F}^{n+s} \in \boldsymbol{X}_n^*$ is given by the right-hand side of (8) and (10) respectively.

The saddle point problem (11) has a unique solution $(\boldsymbol{U}^{n+s}, P^{n+s})$ since A_n is invertible and the Taylor-Hood element is a stable discretization, i.e. the Ladyženskaja-Babuška-Brezzi (LBB) condition

$$\inf_{\Psi \in Y_n \setminus \{0\}} \sup_{\boldsymbol{\Phi} \in \boldsymbol{X}_n \setminus \{\boldsymbol{0}\}} \frac{\int_\Omega \Psi\, \operatorname{div} \boldsymbol{\Phi}\, dx}{\|\Psi\|_{L^2(\Omega)}\, \|\boldsymbol{\Phi}\|_{H^1(\Omega;\mathbb{R}^d)}} \geq \gamma \tag{12}$$

is satisfied with a constant γ which only depends on the minimal angle of the underlying triangulation. A proof of (12) can for instance be found in [25].

The pressure P^{n+s} is the unique solution of

$$B_n^* A_n^{-1} B_n\, P^{n+s} = B_n^* A_n^{-1}\, \boldsymbol{F}^{n+s} \qquad \text{in } Y_n^* \tag{13}$$

and the velocity $\boldsymbol{U}^{n+s}$ is then given as

$$A_n \boldsymbol{U}^{n+s} = \boldsymbol{F}^{n+s} - B_n\, P^{n+s} \qquad \text{in } \boldsymbol{X}_n^*.$$

The *Schur complement operator* $B_n^* A_n^{-1} B_n\colon Y_n \to Y_n^*$ is a symmetric, positive definite operator. Hence, we can use a conjugate gradient method for the numerical solution of (13), as presented in [6].

In finite element methods all operators correspond to sparse matrices due to the finite support of the basis functions. The inverse of a sparse matrix is in general a dense matrix and thus the matrix of $B_n^* A_n^{-1} B_n$ is not stored explicitly. In the conjugate gradient method we do not need the matrix but only the evaluation of $B_n^* A_n^{-1} B_n \Psi$ for some given $\Psi \in Y_n$. This can be done by solving a problem of the form: For given $\Psi \in Y_n$, find $\boldsymbol{\Phi} \in \boldsymbol{X}_n$ such that

$$A_n\, \boldsymbol{\Phi} = B_n\, \Psi \qquad \text{in } \boldsymbol{X}_n^* \tag{14}$$

and then applying B_n^* to $\boldsymbol{\Phi}$.

Since the condition number of $B_n^* A_n^{-1} B_n$ blows up for $\frac{\tau}{Re} \to 0$ we use a preconditioned conjugate gradient algorithm. This ensures that the number of iterations does not depend on these parameters. This preconditioning involves the additional solution of a Laplace equation with Neumann boundary conditions on Γ_D and a Robin boundary condition on Γ_N in the pressure space Y_n, see [4, 6] for details.

3.2.4. *The solution of the non-linear elliptic equation.* Define the linear operators $A_n\colon \boldsymbol{X}_n \to \boldsymbol{X}_n^*$ by

$$\langle A_n \boldsymbol{\Phi}_i,\, \boldsymbol{\Phi}_j \rangle = \frac{1}{\theta' \tau} \int_\Omega \boldsymbol{\Phi}_i\, \boldsymbol{\Phi}_j\, dx + \frac{\beta}{Re_d} \int_\Omega \nabla \boldsymbol{\Phi}_i\, \nabla \boldsymbol{\Phi}_j\, dx$$

for all $i,\, j = 1, \ldots, N_n$ and $D_n\colon \boldsymbol{X}_n \times \boldsymbol{X}_n \to \boldsymbol{X}_n^*$ by

$$\langle D_n(\boldsymbol{V}, \boldsymbol{\Phi}_i),\, \boldsymbol{\Phi}_j \rangle = \int_\Omega \boldsymbol{V} \cdot \nabla \boldsymbol{\Phi}_i\, \boldsymbol{\Phi}_j\, dx$$

for all $\boldsymbol{V} \in \boldsymbol{X}_n$ and $i,\, j = 1, \ldots, N_n$. The finite element discretization of (9) leads to the following non-linear equation for the velocity: Find $\boldsymbol{U}^{n+1-\theta} \in \boldsymbol{g}^{n+1-\theta} + \boldsymbol{X}_n$:

$$A_n \boldsymbol{U}^{n+1-\theta} + D_n(\boldsymbol{U}^{n+1-\theta}, \boldsymbol{U}^{n+1-\theta}) = \boldsymbol{F}^{n+1-\theta} \qquad \text{in } \boldsymbol{X}_n^*, \tag{15}$$

where $\boldsymbol{F}^{n+1-\theta} \in \boldsymbol{X}_n^*$ is given by the right-hand side of (9).

For the numerical solution of this non-linear equation we use the *nonlinear GMRES* method proposed in [4] and [20]. Fix $k \in \mathbb{N}$, and let $\boldsymbol{V}_0$ an initial guess for the discrete velocity ($\boldsymbol{V} = \boldsymbol{U}^{n+\theta}$, e.g.). For $m \geq 0$ compute $\boldsymbol{V}_{m+1} \in \boldsymbol{X}_n$ from $\boldsymbol{V}_m$ by solving the linearized equation

$$A_n \boldsymbol{V}_{m+1} + D_n(\boldsymbol{V}_m, \boldsymbol{V}_{m+1}) = \boldsymbol{F}^{n+1-\theta} \qquad \text{in } \boldsymbol{X}_n^*$$

approximately, i.e. use one step of the GMRES method with restart k and initial guess $\boldsymbol{V}_m$ for the solution of the resulting linear system. If $\boldsymbol{V}_{m+1}$ is a solution of (15) (or, in practice, the residual of the equation is sufficiently small) then set $\boldsymbol{U}^{n+1-\theta} = \boldsymbol{V}_{m+1}$ and stop. Otherwise increment m and do the next iteration.

If the time step size τ is sufficiently small the nonlinear GMRES converges fast in practice (usually 5 to 10 iterations with $k \approx 15$).

3.2.5. *Data transfer during mesh modifications.* During mesh refinement or coarsening we have to transfer $\boldsymbol{U}^n$ from the old grid $\mathcal{T}_{n-1}$ to the new grid $\mathcal{T}_n$. Using the standard nodal interpolation I_n between $\boldsymbol{X}_{n-1}$ and $\boldsymbol{X}_n$, $I_n \boldsymbol{U}^n$ may not be discretely divergence free on the new grid and the term

$$\frac{1}{\theta\, \tau} I_n \boldsymbol{U}^n$$

in the right-hand side of (8) for the fully discrete problem may then lead to strong numerical oscillations in the discrete pressure P.

In order to avoid these oscillations we therefore replace this term by

$$\frac{1}{\theta\, \tau} \Pi_n \boldsymbol{U}^n,$$

where $\Pi_n \boldsymbol{U}^n$ is a projection of the discrete velocity from the old time step onto the space of discretely divergence free functions on the new grid as proposed in [5].

For that let μ, κ be positive constants and define $A_n\colon \boldsymbol{X}_n \to \boldsymbol{X}_n^*$ by

$$\langle A_n \boldsymbol{\Phi}_i,\, \boldsymbol{\Phi}_j \rangle = \mu \int_\Omega \boldsymbol{\Phi}_i\, \boldsymbol{\Phi}_j\, dx + \kappa \int_\Omega \nabla \boldsymbol{\Phi}_i\, \nabla \boldsymbol{\Phi}_j\, dx$$

for all $i,\, j = 1, \ldots, N_n$ and define $\boldsymbol{F} \in \boldsymbol{X}_n^*$ by

$$\mu \int_\Omega \boldsymbol{U}^n\, \boldsymbol{\Phi}_j\, dx + \kappa \int_\Omega \nabla \boldsymbol{U}^n\, \nabla \boldsymbol{\Phi}_j\, dx$$

for all $j = 1, \ldots, N_n$. Solving now a linear saddle point problem for $\Pi_n \boldsymbol{U}^n \in \boldsymbol{g}^n + \boldsymbol{X}_n$ and $Q \in Y_n$ such that

$$\begin{bmatrix} A_n & B_n \\ B_n^* & 0 \end{bmatrix} \begin{bmatrix} \Pi_n \boldsymbol{U}^n \\ Q \end{bmatrix} = \begin{bmatrix} \boldsymbol{F} \\ 0 \end{bmatrix} \qquad \text{in } \boldsymbol{X}_n^* \times Y_n^*,$$

we end up with a discretely divergence free projection $\Pi_n \boldsymbol{U}^n \in \boldsymbol{X}_n$ of $\boldsymbol{U}_n$ which then can be used on the right-hand side of the fully discrete equations of (8). Note that the above projection is nothing else but a generalized Stokes problem for $\Pi_n \boldsymbol{U}^n$.

3.3. **Procedure of the Measurement.** The frequencies in the numerical simulations were obtained in the following way: We analyzed the temporal behaviour of a typical quantity of the flow at a fixed position $x_1 \in \Omega$ after computing for a sufficiently large number of periods. We used x_1, a point $w/5$ left and slightly above the edge of the labium. As quantity we chose the horizontal velocity component $u_1(x_1, \cdot)$ at x_1.

Note that the obtained frequencies do not depend on the specific choice of the quantity or position x_1, since the first harmonic is predominant for this set of values.

$d = 0.5$ mm			$d = 1.0$ mm		
U_0[m/s]	w_{min}–w_{max}[mm]	$S_d(\bar{f})$	U_0[m/s]	w_{min}–w_{max}[mm]	$S_d(\bar{f})$
3.38	3.7 – 7.7	0.027	3.38	6.4 – 8.9	0.044
4.67	3.2 – 6.7	0.027	4.88	4.5 – 7.6	0.057
5.94	2.8 – 6.3	0.040	6.20	4.1 – 6.6	0.057
6.20	2.7 – 6.2	0.040	6.54	4.2 – 7.2	0.061
—	—	—	7.43	3.7 – 6.2	0.067
7.92	2.6 – 5.3	0.040	8.18	4.0 – 6.7	0.066
9.77	2.3 – 4.8	0.046	9.78	3.7 – 6.5	0.070
11.12	2.3 – 4.5	0.050	11.34	3.5 – 6.0	0.076
12.60	2.3 – 4.3	0.050	13.04	3.5 – 5.7	0.077

TABLE 1. The essential parameters of the experiment: the velocity U_0 of the center of the jet at the flue exit, the range of the stand-off distance w used for the fit and the average Strouhal number S_d of the mean frequency measured, respectively.

4. Experimental and Numerical Investigation

4.1. **Experimental Investigation.** A number of test runs precede the measurements described here in order to explore the reliability of the conditions. This concerns higher velocities than quoted below and also larger distances w. Especially larger distances show the expected higher hydro dynamical modes and their frequency dependence are very similar to the first mode. The frequency near the transition to the higher mode is lower by about 10% as compared with the $1/w$-parametrization.

The measurements are performed as a variation in w in steps of 0.5 mm at the velocities given in Table 1. The corresponding Reynolds numbers Re_d range between 113 and 416 for $d = 0.5$ mm and between 225 and 873 for $d = 1.0$ mm. Note that for the ease of presentation in this table only average Strouhal numbers (from average frequencies $\bar{f}$) are listed. In the comparison with the simulations in Figure 5 all measuered frequencies enter individually.

4.2. **Numerical investigation.** We perform the numerical simulations for all combinations of values for $w = 2.5, 3.0, 3.5, 4.0, 4.5$ [mm], $U_0 = 5.25, 7.00, 8.75, 10.50, 12.25, 14.00$ [m/s] and $d = 0.5, 1.0$ [mm]. The offset is $\varepsilon = 0.2$ mm for $d = 0.5$ mm and $\varepsilon = 0.4$ mm for $d = 1.0$ mm respectively. The results of the simulations are listed in Table 2. The corresponding Reynolds numbers Re_d range between 171 and 456 for $d = 0.5$ mm and between 343 and 912 for $d = 1.0$ mm. In this table the Strouhal number is given for each setting of the stand-off distance w.

As can be seen from Table 2 the frequencies behave quite well for most cases of the chosen parameters. There are only some limiting cases, where no reasonable frequencies could be obtained: For $d = 0.5$ mm the flow becomes more chaotic for bigger values of w and U_0. For instance in the case $w = 4.5$ mm and $U_0 = 14.00$ m/s the flow is no longer periodic or quasi periodic, so that no single frequency could be extracted any more. In the case $d = 1.0$ mm the system does not oscillate for small values of w and U_0, see Table 2.

$d = 0.5$ mm			$d = 1.0$ mm		
U_0 [m/s]	w [mm]	$S_d(f)$	U_0 [m/s]	w [mm]	$S_d(f)$
5.25	2.5	0.052	5.25	2.5	—
	3.0	0.042		3.0	0.094
	3.5	0.036		3.5	0.080
	4.0	0.031		4.0	0.073
	4.5	0.028		4.5	0.064
7.00	2.5	0.055	7.00	2.5	—
	3.0	0.045		3.0	—
	3.5	0.039		3.5	0.085
	4.0	0.034		4.0	0.076
	4.5	0.029		4.5	0.068
8.75	2.5	0.057	8.75	2.5	—
	3.0	0.047		3.0	0.097
	3.5	0.041		3.5	0.086
	4.0	0.037		4.0	0.077
	4.5	0.030		4.5	0.070
10.50	2.5	0.059	10.50	2.5	0.111
	3.0	0.049		3.0	0.100
	3.5	0.043		3.5	0.087
	4.0	0.036		4.0	0.078
	4.5	0.034		4.5	0.070
12.25	2.5	0.061	12.25	2.5	0.117
	3.0	0.051		3.0	0.100
	3.5	0.045		3.5	0.090
	4.0	0.040		4.0	0.079
	4.5	0.035		4.5	0.072
14.00	2.5	0.062	14.00	2.5	0.116
	3.0	0.053		3.0	0.103
	3.5	0.045		3.5	0.092
	4.0	0.038		4.0	0.079
	4.5	—		4.5	0.072

TABLE 2. Parameters of the simulation: the maximal inflow velocity of the the jet U_0, the stand-off distance w, Strouhal number S_d of the frequency.

4.3. **Evaluation and comparison.** The considered Reynolds numbers Re_d with respect to the height d are between 113 and 873 for the experiment and between 171 and 912 for the simulation; note that the Reynolds number with respect to the stand-off distance would typically be larger by a factor 5 to 8. The corresponding frequencies for both the experiment and simulation are displayed in Figure 5.

Along with the measured values of the frequency the dependence of the scaling law (3) with $n = 1$

$$f = C_d \frac{U_0}{w} \tag{16}$$

is displayed with a global factor being fitted to given data. The following values have been determined in the experiment:

$$\bar{C}_{d=0.5\text{ mm}} = 0.33 \pm 0.02 \qquad \text{and} \qquad \bar{C}_{d=1.0\text{ mm}} = 0.35 \pm 0.02.$$

The error quoted is mainly due to the velocity determination in this experiment. It should be mentioned that several preceding runs yield results which are consistent.

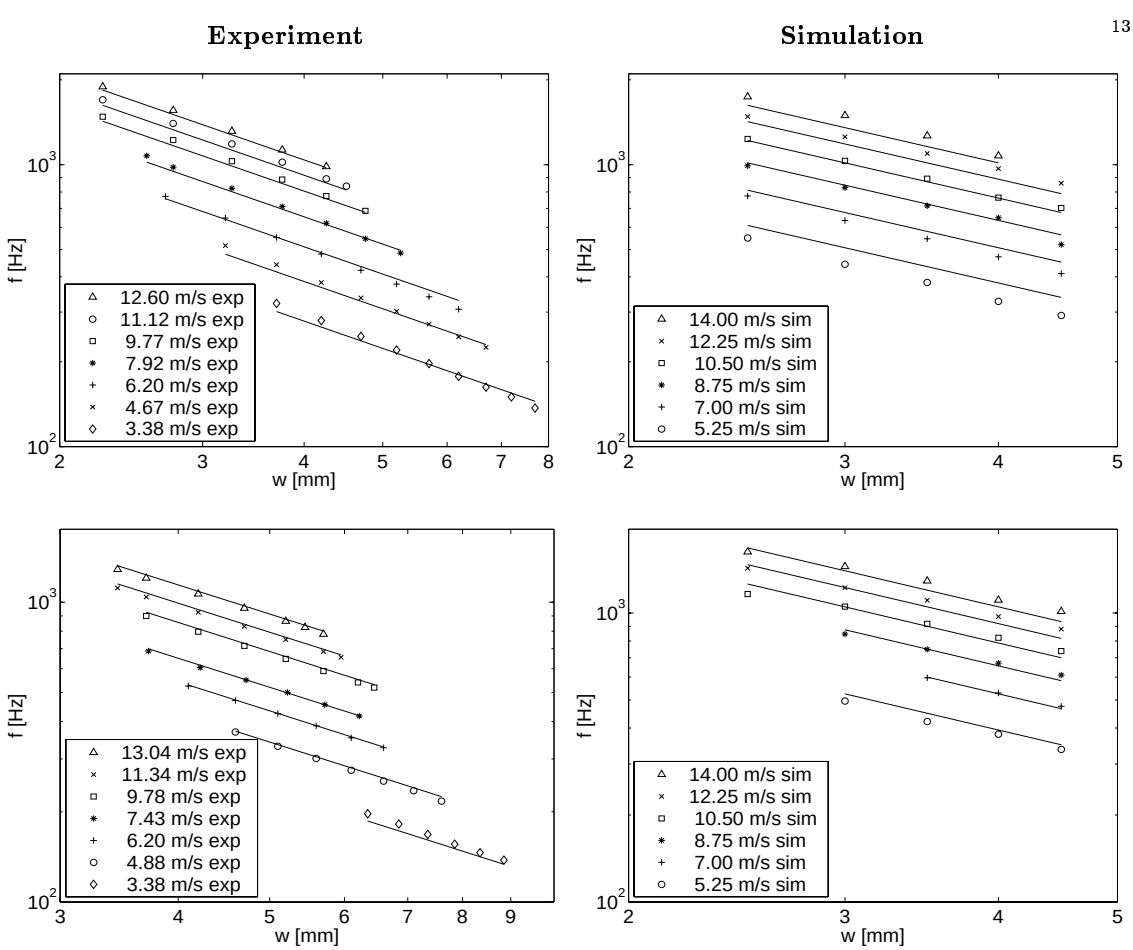

FIGURE 5. Frequencies f versus stand-off distance w from experiment and simulation. Top: $d = 0.5$ mm, bottom: $d = 1.0$ mm. The solid lines are the fitted curves according to (16) with the experimental and numerical values of $\bar{C}_{d=0.5\ \mathrm{mm}}$ and $\bar{C}_{d=1.0\ \mathrm{mm}}$, respectively.

By the simulation we have computed the following average values for $\bar{C}_d$:

$$\bar{C}_{d=0.5\ \mathrm{mm}} = 0.29 \pm 0.04 \qquad \text{and} \qquad \bar{C}_{d=1.0\ \mathrm{mm}} = 0.30 \pm 0.03.$$

In general, there is an excellent agreement between experiment and simulation:

- There is a good proportionality of the frequency with the velocity for both, the experiment and the simulation.
- There is almost no deviation from the simple law with $n = 1$. It should be mentioned that this statement holds also for the higher hydro dynamical modes.
- The constants C are almost the same, i.e. $\bar{C}_{d=0.5\ mm}/\bar{C}_{d=1.0\ mm} = 0.96 \pm 0.02$ in the experiment and $\bar{C}_{d=0.5\ mm}/\bar{C}_{d=1.0\ mm} = 0.96 \pm 0.11$ in the simulation.

The following remarks concern further observations:

- The agreement of experiment and simulation for the absolute value of the constants C_d within 10–15% is remarkable.
- Assuming a $f \sim (1/w)^n$-dependence the results of our investigation might suggest that $n > 1$ and therefore giving rise to $\bar{C}_{d=0.5\ mm}/\bar{C}_{d=1.0\ mm} < 1$, which is indeed observed.

- There is a distinct difference between experiment and simulations concerning the threshold for the distance w where oscillations occur: especially at low velocities and for $d = 1$ mm the regime of the oscillation of the first hydro dynamic mode is shifted to smaller values of w in the simulation. The onset of oscillations is certainly influenced by noise which is not treated explicitly in these investigations.

The result of the simple scaling law with $n = 1$ deserves a closer look. There is an indication in the publication of Mattingly and Criminale [21], which leads to the correct power dependence: Dispersion relations from the linearized fluid dynamical equations show a steeply increasing phase velocity at low Strouhal numbers, but flattens out at $S_d > 0.016$. These calculations were done with the Bickley velocity profile

$$U(y) = \frac{U_0}{\mathrm{sech}^2(2y/d)}.$$

Under the approximation of a *constant* phase velocity the exponent would be $n = 1$, indeed.

There might be a concern about a possible dependence of the exponent of the scaling law on the velocity profile at the exit of the flue. It should be mentioned that the dependence of the real part of the dispersion relation on various velocity profiles was determined recently by numerical solutions of the linearised problem by H. Preckel [27]. There, it is shown that the dependence of the real part of the wave number, and therefore of the phase velocity on the velocity profile of the jet is small even if the shape approaches a top hat profile. Indeed, in our experimental setup a situation of a top hat profile was produced by forming a nozzle with two razor blades. From these measurements a constant $\tilde{C}$ could be deduced which is very similar to the constant obtained with the parabolic profile.

Finally, we present some pictures from the experiment and simulation. Figure 6 shows a visualization of the jet in a special experimental setup using the 'Schlieren method' with stroboscopic illumination for $d = 1$ mm. As medium for the jet carbon dioxide is used. The 'Schlieren method'

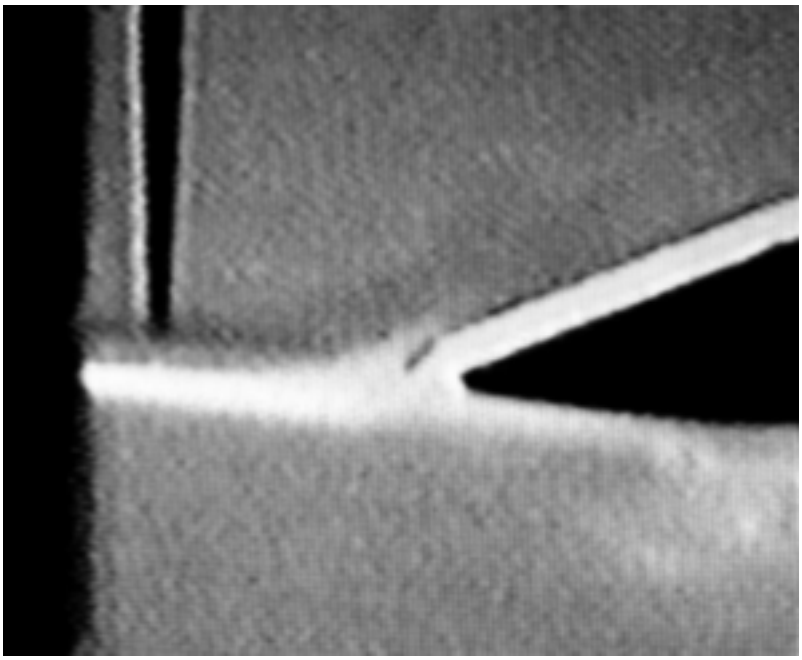

FIGURE 6. Experimental setup for $d = 1$ mm. The visualisation of the jet is achieved by the 'Schlieren method'. The picture shows the hot wire anemometer in the retracted position.

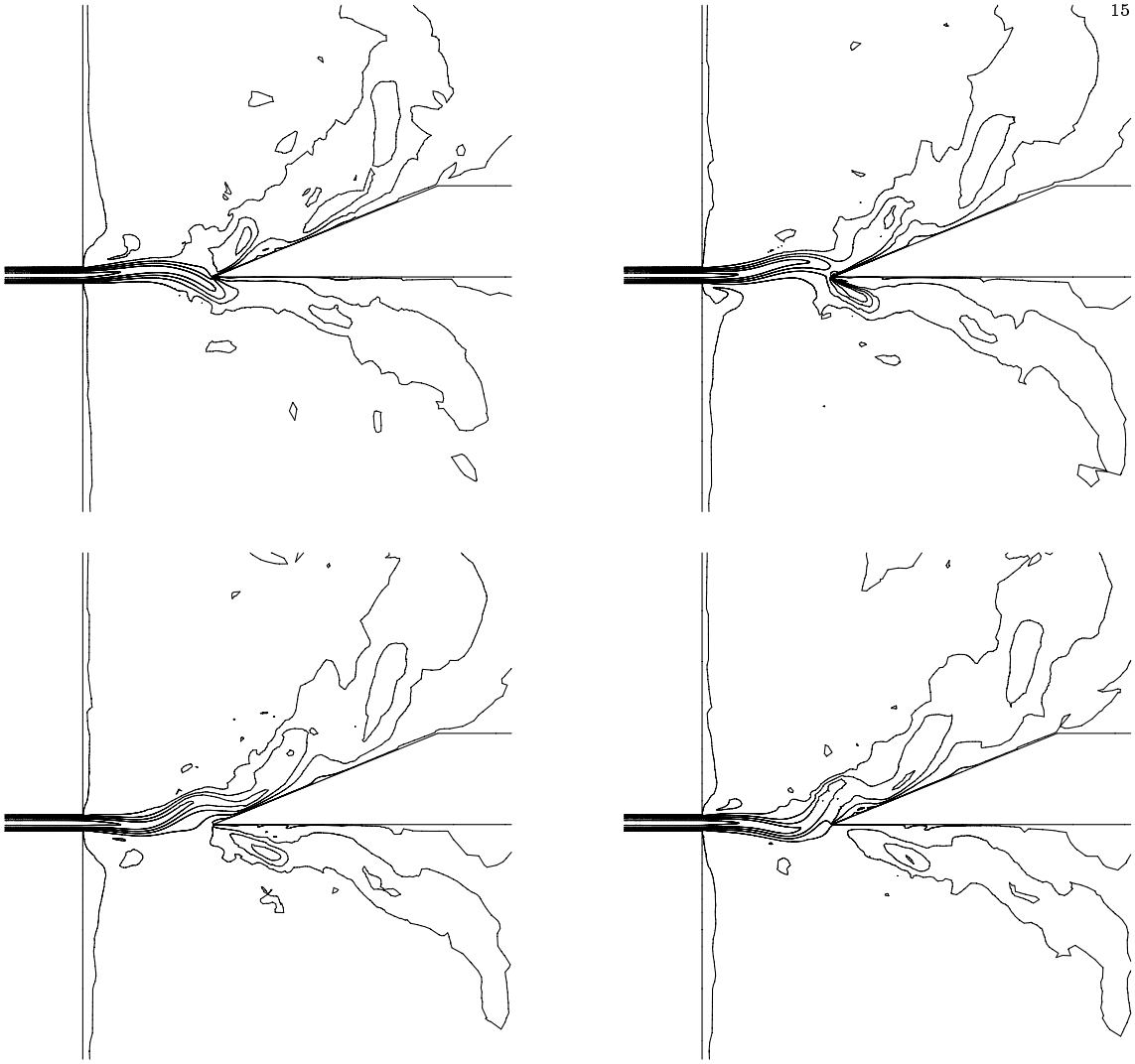

FIGURE 7. Modulus of the velocity at some t_0, $t_0 + 0.5$ [10^{-3}s], $t_0 + 1.0$ [10^{-3}s] and $t_0 + 1.5$ [10^{-3}s] respectively.

visualizes the jet shape using the change of the refractive index compared to the surrounding air. The hot wire anemometer is seen near the exit of the flue positioned at the retracted position used for the frequency measurement. The jet oscillates around the horizontal axis given by the free jet in case the edge is removed. During the experiment, edge vortices are observed above and below the edge, being 180° out of phase to each other. In the picture, the vortex is below the edge during the downward movement of the jet.

The last pictures refer to the simulations. Figure 7 and Figure 8 show 4 time instants of the flow for $d = 0.5$ mm and $w = 4.0$ mm. In Figure 7 isolines of the modulus of the velocity are displayed, while in Figure 8 the difference $u - U$ is plotted, where U is the time averaged velocity, defined by $U(x) := \frac{1}{T}\int_0^T u(x,t)\,dt$, T sufficiently large. Both figures underline the highly transient character of the flow. Figure 9 shows a phase diagram $u_1(x_2,\cdot)$ versus $u_1(x_1,\cdot)$ with x_2 a point $w/5$ left of x_1 demonstrating the periodic behaviour of the flow. A typical adaptive mesh (with a zoom to the region in between inlet and labium) from the simulation can be seen in Figure 10. These pictures clearly demonstrate the benefit from an adaptive methods: the grid has only a high

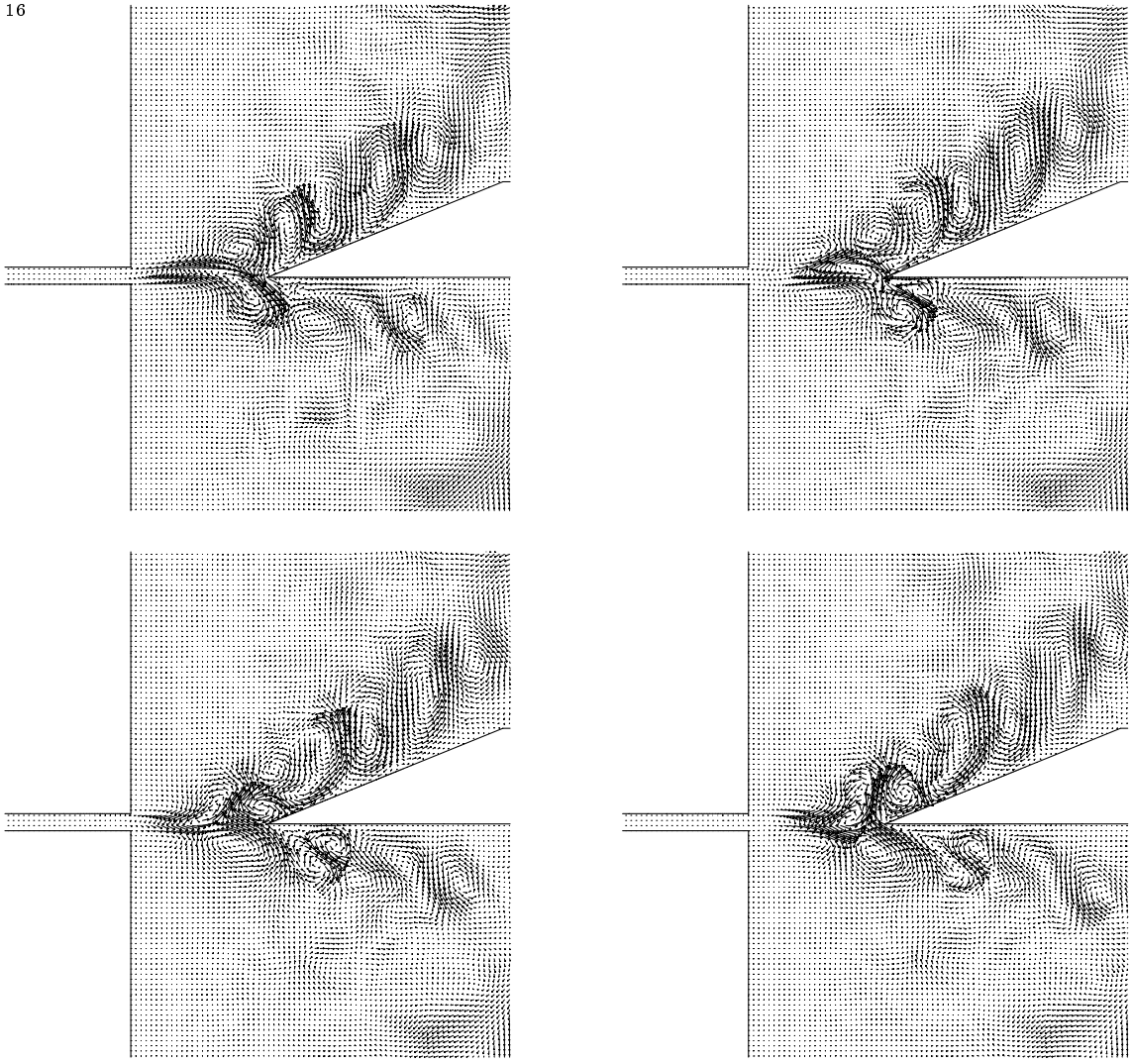

FIGURE 8. Difference $u-U$ at some t_0, $t_0+0.5\,[10^{-3}\mathrm{s}]$, $t_0+1.0\,[10^{-3}\mathrm{s}]$ and $t_0+1.5\,[10^{-3}\mathrm{s}]$ respectively.

resolution where needed (near the tip of the labium) while it is rather coarse in all other parts of the computational domain.

5. Summary

In this paper we have investigated the edge tone phenomena by both, experiment and numerical simulation. Main focus was the determination of the exponent n in (3). Only the use of adaptive finite elements made the simulations feasible and results in an excellent agreement of the experimental and numerical determination of this exponent. We have shown that this exponent has a $n = 1$ behaviour for the Reynolds numbers considered in this investigation. All other efforts for deriving the law (3) from first principles without input, which is either deduced from experiment or adjusted by hand, do not yield the right behaviour. Moreover the agreement of experiment and simulation for the absolute value of the constants C_d within 10–15% is remarkably good.

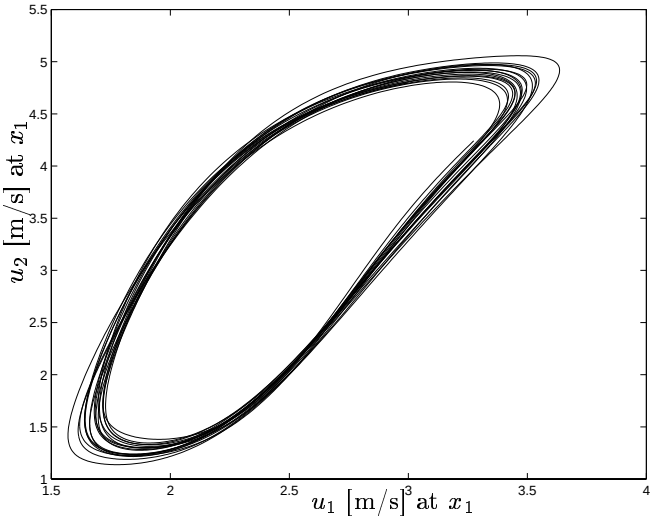

FIGURE 9. Phase diagram.

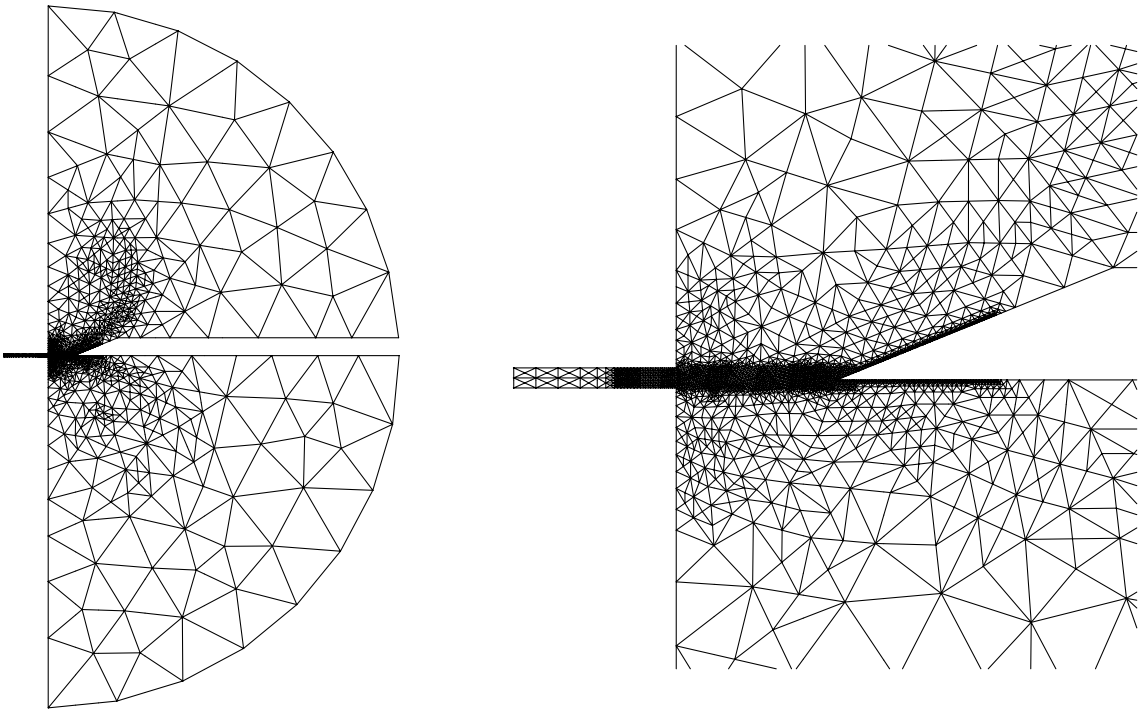

FIGURE 10. Typical adaptive finite element mesh; right: close up.

REFERENCES

[1] J. B. BRACKENRIDGE, *Transverse oscillations of a liquid jet*, J. Acoust. Soc. Am., vol. 32 (1960), p. 1237.

[2] E. BÄNSCH, *An adaptive finite–element strategy for the three–dimensional time–dependent Navier–Stokes equations*, J. Comput. Appl. Math., 36 (1991), pp. 3–28.

[3] ———, *Local mesh refinement in 2 and 3 dimensions*, IMPACT Comput. Sci. Engrg., 3 (1991), pp. 181–191.

[4] ———, *Simulation of instationary, incompressible flows*, Acta Math. Univ. Comenianae LXVII, no. 1 (1998), pp. 101–114.

[5] E. Bänsch and A. Schmidt, *Simulation of dendritic crystal growth with thermal convection*, Interfaces and Free Boundaries, 2 (2000), pp. 95–115.
[6] M. O. Bristeau, R. Glowinski, and J. Periaux, *Numerical methods for the Navier–Stokes equations. Applications to the simulation of compressible and incompressible viscous flows*, Computer Physics Reports, 6 (1987), pp. 73–187.
[7] G. B. Brown, *The vortex motion causing edge tones*, Proc. Phys. Soc. 49 (1937), p. 493.
[8] Z. Carriere, *Phénomènes a l'embouchure d'un tuyau d'orgue*, J. d Phys. et Rad., vol. 6 (1924), p. 52.
[9] M. Castellongo, *Acoustical analysis of initial transients in flute like instruments*, Acta Acustica, vol. 85 (1999), p. 1.
[10] D. G. Crighton, *The jet edge-tone feedback cycle; linear theory for the operating stages.* J. Fluid Mech., vol. 234 (1992), p. 361.
[11] P. G. Drazin and W. H. Reid, *Hydrodynamic stablility of parallel flow of inviscid fluid* Adv. Apppl. Mech. 7 (1966), pp. 142 - 152.
[12] E. Fernandez–Cara, M.M. Beltran, *The Convergence of two Numerical Schemes for the Navier–Stokes Equations*, Numer. Math. 55 (1989), pp. 33–60.
[13] J. G. Heywood, R. Rannacher, and S. Turek, *Artificial boundaries and flux and pressure conditions for the incompressible Navier-Stokes equations.*, Int. J. Numer. Methods Fluids, 22 (1996), pp. 325–352.
[14] D. K. Holger et al., *Fluid dynamics of the edgetone.* J. Acoust. Soc. Am., 62 (1977), p. 1116.
[15] M. S. Howe, *Raleigh conductivity and self-sustained oscillations* Theoretical and Computational Fluid Dynamics 10 (1998), pp. 187 - 200.
[16] A. T. Jones, *Edge tones*, J. Acoust. Soc. Am., vol. 14 (1942), p. 131.
[17] P. Kloucek, F. Rys, *Stability of the fractional step θ–scheme for the nonstationary Navier–Stokes equations,* SIAM J. Numer. Anal., vol. 31, no. 5 (1994), pp. 1312–1335.
[18] Yong-Pil Kwon, *Phase-locking condition in the feedback loop of low-speed edgetones* JASA 100 (1996), pp. 3028-3032
[19] M. Lesieur, *Turbulence in Fluids*, Kluwer Academic Publisher 1993.
[20] M. Mallet, J. Periaux, and B. Stoufflet, *Convergence acceleration of finite element methods for the solution of the Euler and Navier–Stokes equations of compressible flow*, in Proc. 7th GAMM-Conf., Louvain-La-Neuve/Belg. 1987, vol. 20 of Notes Numer. Fluid Mech., 1988, pp. 199–210.
[21] G.E. Mattingly, W.O. Criminale, *Disturbance characteristics in a plane jet*, The Physics of Fluids, vol. 14, (1971), p. 2258.
[22] S. Müller-Urbaniak, *Analysis of the fractional step θ-scheme for the solution of the instationary Navier–Stokes equations.* (In German) University of Heidelberg, Preprint 94-01, 1994.
[23] W. Nolle, *Sinuous instability of a planar air jet: Propagation parameters and acoustic excitation* JASA Vol. 103 (1998), pp. 3690 - 3705.
[24] W. L. Nyborg et al., *Acoustical characteristics of the jet-edge and jet-edge-resonator systems*, Journ. Acoust. Soc. Am., vol. 52 (1952), p. 293.
[25] F. Otto, *On the Babuška–Brezzi condition for the Taylor–Hood element.* (In German) Master thesis, University of Bonn (1990).
[26] A. Powell, *On edge tones and associated phenomena.* Acoustica 3 (1953), p. 233.
[27] H. Preckel, *Dynamische Steuerung der Strahl-Kanten-Strömung.* Universität Göttingen, PhD Thesis, 1999.
[28] J. E. Rossiter, *The effect of cavities on the buffeting of the aircraft*, Royal Aircraft Establishment Technical Memorandum 745 (1962).
[29] H. Sato and K. Kuriki, *The mechanism of transition in the wake of a thin flat plate placed parallel to a uniform flow* J. of Fluid Mech. 224 (1961), pp. 133 - 158.
[30] A. Schmidt and K. G. Siebert, *ALBERT: An adaptive hierarchical finite element toolbox.* Preprint 06/2000 Freiburg, 2000. Documentation, 244 p.
[31] C. Sondhauss, *Über die beim Ausströmen der Luft entstehenden Töne*, Ann. Phys. 91 (1854), p. 128.
[32] R. Verfürth, *A review of a posteriori error estimation and adaptive mesh-refinement techniques.*, Wiley & Sons, Teubner, 1996.